AGU PUBLICATIONS

JGR

Journal of Geophysical Research: Solid Earth

RESEARCH ARTICLE
10.1002/2017JB014848

Key Points:
- Critical step over jump distance is controlled by seismogenic depth and background stress
- Critical step over distance is slightly dependent on nucleation size
- Earthquakes may jump wider step overs on faults with thicker seismogenic zone or operating at higher stress

Correspondence to:
K. Bai,
kbai@caltech.edu

Citation:
Bai, K., & Ampuero, J.-P. (2017). Effect of seismogenic depth and background stress on physical limits of earthquake rupture across fault step overs. *Journal of Geophysical Research: Solid Earth*, *122*, 10,280–10,298. https://doi.org/10.1002/2017JB014848

Received 10 AUG 2017
Accepted 9 NOV 2017
Accepted article online 15 NOV 2017
Published online 23 DEC 2017

Effect of Seismogenic Depth and Background Stress on Physical Limits of Earthquake Rupture Across Fault Step Overs

Kangchen Bai[1] **and Jean-Paul Ampuero**[1]

[1] Seismological Laboratory, California Institute of Technology, Pasadena, CA, USA

Abstract Earthquakes can rupture geometrically complex fault systems by breaching fault step overs. Quantifying the likelihood of rupture jump across step overs is important to evaluate earthquake hazard and to understand the interactions between dynamic rupture and fault growth processes. Here we investigate the role of seismogenic depth and background stress on physical limits of earthquake rupture across fault step overs. Our computational and theoretical study is focused on the canonical case of two parallel strike-slip faults with large aspect ratio, uniform prestress and friction properties. We conduct a systematic set of 3-D dynamic rupture simulations with different seismogenic depth, step over distance, and initial stresses. We find that the maximum step over distance H_c that a rupture can jump depends on seismogenic depth W and strength excess to stress drop ratio S, commonly used to evaluate probable rupture velocity, as $H_c \propto W/S^n$, where $n = 2$ when $H_c/W < 0.2$ (or $S > 1.5$) and $n = 1$ otherwise. The critical nucleation size, largely controlled by frictional properties, has a second-order effect on H_c. Rupture on the secondary fault is mainly triggered by the stopping phase emanated from the rupture end on the primary fault. Asymptotic analysis of the peak amplitude of stopping phases sheds light on the mechanical origin of the relations between H_c, W, and S, and leads to the scaling regime with $n = 1$ in far field and $n = 2$ in near field. The results suggest that strike-slip earthquakes on faults with large seismogenic depth or operating at high shear stresses can jump wider step overs than observed so far in continental interplate earthquakes.

1. Introduction

Earthquakes often occur on fault systems with multiple strands separated by step overs. These discontinuities can act as barriers that arrest earthquakes ruptures, but this is not always the case: ruptures can also jump across step overs. For example, the 2013 M_w7.7 Balochistan earthquake rupture stopped at a dilational step over at its southern end (Zhou et al., 2016), whereas the 1992 M_w7.3 Landers earthquake breached four major step overs within the Eastern California Shear Zone (Sieh et al., 1993).

Understanding the role of step overs on rupture propagation and arrest has both practical and fundamental significance. An important mechanism by which earthquakes become large is by breaking multiple fault segments, despite the structural barriers that separate them (Hamling et al., 2017; Meng et al., 2012; Sieh et al., 1993). In seismic hazard analysis, the likelihood of multiple fault segments rupturing during a single earthquake is a crucial consideration to determine the largest expected magnitude in a complex fault system (Field et al., 2014). An important goal is to establish quantitative relations between the efficiency of step over jumps and the geometrical properties of step overs. Efforts to achieve this goal empirically have yielded seminal results (e.g., Biasi & Wesnousky, 2016; Wesnousky, 2006; Wesnousky & Biasi, 2011) but are ultimately limited by the small number of earthquakes with sufficient rupture and fault observations. Mechanical models can offer a complementary support to such efforts, for instance, by providing mechanically motivated functional forms to guide the development of empirical relations and physically expected bounds to supplement empirical models.

Step overs and other geometrical features of faults are also the subject of basic research, especially on the relation between the short timescales of dynamic rupture and the long timescales of fault growth. The dynamic generation of damage and branching during earthquake rupture contributes to the long-term evolution of fault zones (Ampuero & Mao, 2017; Cooke, 1997; Herbert et al., 2014). One mechanism of fault growth

operates by coalescence of multiple fault segments during which the step overs are breached (de Joussineau & Aydin, 2007). If the two neighboring fault segments interact strongly throughout their earthquake cycles, simultaneous modeling of the whole fault system is required.

Continental strike-slip earthquakes rarely manage to jump step overs larger than about 5 km (Elliott et al., 2009; Wesnousky, 2006; Xu et al., 2006). This has been also observed in dynamic rupture simulations (Harris et al., 1991; Harris & Day, 1999; Lozos et al., 2014, 2015; Oglesby, 2005) even if the second fault segment is very close to failure. A critical step over distance $H_c = 5$ km has been incorporated in seismic hazard assessment models such as the Third Uniform California Earthquake Rupture Forecast (Field et al., 2014).

However, some recent earthquakes may have jumped step overs much wider than 5 km. The 2010 M_w7.2 El Mayor-Cucapah earthquake ruptured a 120 km long multisegment fault jumping through an apparent step over of more than 10 km with the possible aid of intermediary fault segments (Oskin et al., 2012; Wei et al., 2011). During the 2012 M_w8.6 Indian Ocean earthquake, the rupture propagated through a complicated orthogonal conjugate fault system. In the late part of this earthquake, back-projection rupture imaging revealed a step over jump as wide as 20 km (Meng et al., 2012). The 2016 M_w7.8 Kaikoura, New Zealand earthquake made an apparent jump through a compressional step over of 15 km (Hamling et al., 2017) taking advantage of several linking faults, which have not been previously mapped for hazard assessment. A common feature of the latter two events is their particularly large rupture depth extent, compared to other strike-slip events. The Indian Ocean earthquake has a centroid depth beyond 25 km; its rupture penetrated into the upper mantle. These observations call for a reexamination of the factors affecting the critical step over distance. Existing models of the efficiency of step over jumps do not account for the role of key observable physical parameters, such as the seismogenic depth, and poorly constrained frictional parameters, such as fracture energy. With ongoing advance in earthquake data gathering and source inversion methods, this information can be obtained and help in generating a more accurate model.

In this computational and theoretical study, we determine key physical parameters that control the critical step over distance in large strike-slip ruptures using numerical simulations and asymptotic analysis. We keep the model as simple as possible so that we can use fracture mechanics arguments to gain physical insight on the numerical modeling results.

2. Model

We consider two vertical, parallel strike-slip faults in a 3-D homogeneous isotropic elastic half-space, as depicted in Figure 1. The elastic medium has density 2,700 kg/m^3, P wave speed 6,000 km/s and S wave speed 3,464 km/s. The faults have length L, seismogenic width W, step over distance H (distance between the two fault traces), and overlapping length D. In our simulations L and D are fixed, while other parameters are variable. We focus on large-magnitude strike-slip earthquakes whose rupture area have large aspect ratio L/W. The regional stress is assumed homogeneous, resulting in a uniform normal stress of $\sigma_0 = 150$ MPa on the faults and uniform shear stress τ_0 whose value is a model parameter. The faults are governed by the linear slip-weakening friction law (Andrews, 1976; Ida, 1972; Palmer & Rice, 1973), with uniform static and dynamic friction coefficients $\mu_s = 0.677$ and $\mu_d = 0.373$, respectively, and critical slip-weakening distance $D_c = 0.5$ m.

Surface-induced supershear rupture (Kaneko et al., 2008) and nucleation at the free surface on the secondary fault (Harris & Day, 1999) can substantially increase H_c for supershear ruptures (Hu et al., 2016, see also section 3.2). These two phenomena have been reported in numerical simulations but not in earthquake observations. They are thus suppressed in this study by setting a negative strength drop in the top 1 km of both faults. A linear slip-weakening friction with negative strength drop mimics rate-and-state friction with velocity strengthening behavior, which Kaneko et al. (2008) adopted to suppress the free surface effect. Laboratory experiments indicate that unconsolidated fault gouge at shallow depth exhibit velocity-strengthening frictional properties (Ikari et al., 2009; Marone & Scholz, 1988).

Earthquake ruptures with large aspect ratio eventually turn into pulse-like ruptures because of the no-slip constraint at the bottom of the seismogenic zone (Ampuero & Mao, 2017; Day, 1982). Their rise time is controlled by stopping phases emanating from the lower limit of the seismogenic layer. Their rupture fronts tend to become straight and vertical at large propagation distance. When such a vertical rupture front suddenly changes speed, especially when it hits the vertical edge of the fault and comes to a stop, it generates stronger

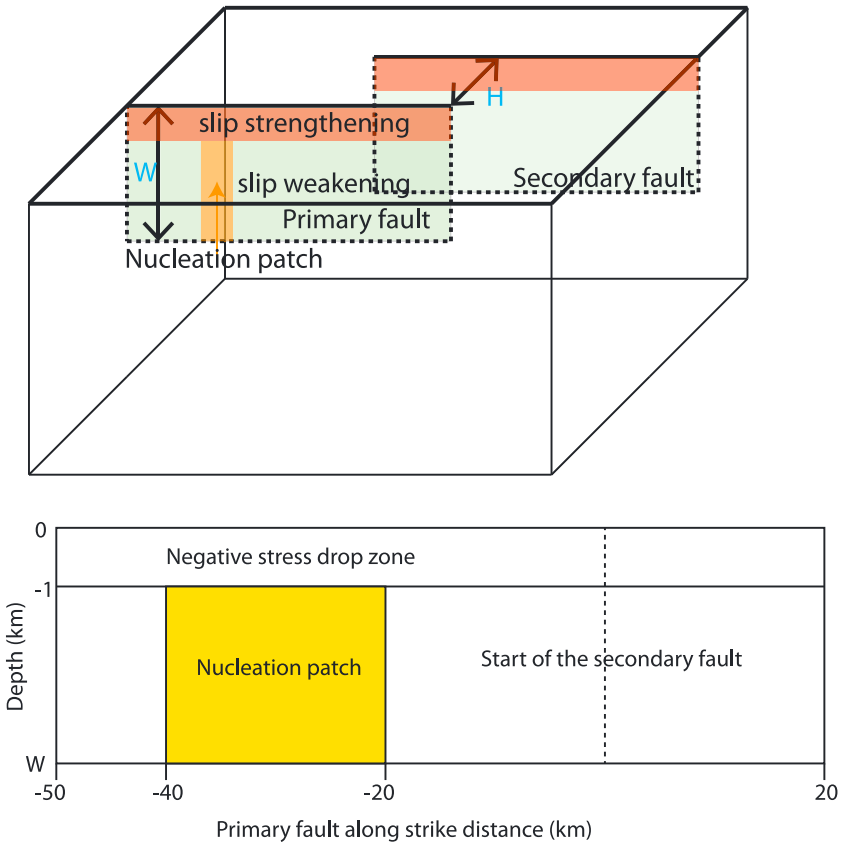

Figure 1. Canonical model of two parallel, vertical strike-slip faults with a step over. (top) Three-dimensional view. The step over distance is H and seismogenic depth is W. (bottom) Side view. Nucleation is enforced on the primary fault in a rectangular area that covers the whole seismogenic depth. A shallow zone of negative strength drop is prescribed.

coherent high-frequency radiation than, for instance, a circular front (Madariaga et al., 2006). The short rise time of a pulse-like rupture further enhances its high-frequency radiation. Hence, the large aspect ratio of large ruptures exacerbates the dynamic stresses that promote step over jumps. However, theoretically, when L/W is so large that the rupture becomes a stationary pulse, the radiation strength of the stopping phase no longer depends on rupture length (Day, 1982). Here we are interested in upper bounds on critical step over distance; hence, we consider the limiting case of very elongated ruptures and adopt an artificial nucleation procedure that favors straightness of the rupture front.

To facilitate the application of our numerical model to different scales, we introduce the following dimensionless quantities. The ratio of strength excess to stress drop, as introduced by (Das & Aki, 1977)

$$S = \frac{\mu_s \sigma_0 - \tau_0}{\tau_0 - \mu_d \sigma_0}, \tag{1}$$

quantifies the relative fault prestress level. The seismogenic depth is characterized by the ratio W/L_c, where the length

$$L_c = \frac{\mu D_c}{\sigma_0(\mu_s - \mu_d)} \tag{2}$$

is representative of the static process zone size, where shear modulus $\mu = 32.4$ GPa. We fix the ratio L/L_c to a large enough value to allow the rupture on the primary fault evolve toward a nearly constant speed. Increasing the rupture acceleration distance has been previously found to increase the critical step over distance (Hu et al., 2016). This can be explained by the fact that before reaching stationary propagation, the peak slip rate of the slipping pulse keeps increasing (Day, 1982), making the potential stopping phase stronger as fault length increases.

Ruptures are initiated by an artificial nucleation procedure intended to minimize the curvature of the primary rupture front, which facilitates step over jumps. We abruptly and simultaneously reduce the coefficient

of friction to its dynamic value within a vertical band extending through the full seismogenic thickness on the primary fault. The horizontal width of this initiation band is set to 20 km in this study by trial and error, to make sure that the rupture with the largest S ratio considered here ($S = 4$) can successfully nucleate on the primary fault. However, a preferred approach to set the size of the initiation zone can be derived from the accurate theoretical estimates developed for nucleation by overstressed regions by Galis et al. (2015).

The step over geometry is characterized by the dimensionless step over distance H/W and overlap distance D/L. A previous study has shown a positive relation between the critical step over distance H_c and D (Harris & Day, 1999). We fix D/L to a large value (0.4) to ensure that the secondary fault is fully exposed to the stress change caused by the primary rupture. Our choices of values for $L/L_c = 140$ and $D/L = 0.4$ favor rupture across the step over and are intended to yield an upper bound estimate of H_c/W.

Dimensional analysis of this basic problem indicates a relation between dimensionless quantities of the form

$$H_c/W = f(S, W/L_c) \tag{3}$$

Here we conduct a systematic set of 3-D dynamic rupture simulations to characterize the yet unknown function f. We scan a range of values of H/W and W/Lc by varying W and H while holding L_c fixed. For each pair $(H/W, W/L_c)$ we use binary search to find the maximum S ratio (S_c) that allows the step over to be breached.

The main focus of this study is on sub-Rayleigh ruptures (propagating slower than Rayleigh wave speed). For supershear ruptures (propagating faster than S wave speed), we did not fully explore the parameter space. Supershear ruptures account for a small amount of events in earthquake observations, and their dynamics can be more complicated. We nevertheless considered several supershear cases for comparison with their sub-Rayleigh counterparts.

We use the spectral element method software SPECFEM3D (Komatitsch & Tromp, 1999). To enable this work, we extended the dynamic rupture solver implemented by Galvez et al. (2014) to take advantage of GPU acceleration (Komatitsch et al., 2010). We use fifth-order spectral elements. Far from the fault we use a coarse mesh with element size of 800 m. Within 10 km of the fault plane we refine the mesh down to an element size of 266 m on the fault, equivalent to an average node spacing of 66.5 m. The mesh resolves well the static process zone size $\approx L_c$ (355 m).

3. Simulation Results

3.1. Effects of Seismogenic Depth W and Strength Excess Ratio S on Critical Step Over Distance

We vary W from 5 to 20 km with increments of 2.5 km and vary H from 0.5 to 3.5 km with increments of 0.5 km. This range of values covers the representative range of most strike-slip earthquakes. For each (W, H) pair, the maximum S value enabling step over jumps is determined by binary search with an accuracy of 0.1 MPa. The resulting critical S_c values for all W and H are shown in Figure 2. The complete set of simulations includes both ruptures that propagated at sub-Rayleigh speed and at supershear speed on the first fault. For a given (W, H) pair, as S is decreased, the following regimes are observed in most cases: sub-Rayleigh rupture without step over jump, sub-Rayleigh with jump, supershear without jump, and finally supershear with jump. We then report in Figure 2 the two maximum S values that yield a step over jump in sub-Rayleigh ruptures (circles) and in supershear ruptures (diamonds), respectively. There are also cases where one regime is missing and the sequence at decreasing S is as follows: sub-Rayleigh without jump, supershear without jump, and supershear with jump. We did not determine S_c for these cases (open circles in Figure 2).

A characteristic pattern is found in the step over jump behavior of sub-Rayleigh ruptures. The S_c values for the sub-Rayleigh cases are plotted separately in Figure 3, which points to a relation of the form $H/W \approx f(S_c)$. The slope of the contours decreases with S_c, indicating that f is a decreasing function. This result can be reinterpreted as a relation between the critical step over distance H_c and W for a fixed S value: $H_c/W \approx f(S)$, in which the ratio H_c/W is lower for larger S.

Further quantitative examination of the simulation results reveals the dependence of H_c/W on S and L_c/W. Based on the results presented in Figure 2 and following the dimensional analysis leading to equation 3, we present in Figure 4 the dependence of the ratio H_c/W on S and L_c/W. In compressional step overs, we find that H_c/W is roughly proportional to $1/S^2$ when S is large. At low S the sub-Rayleigh and supershear cases are clearly separated: for a given S value, sub-Rayleigh ruptures have larger H_c than supershear ruptures. The supershear subset has H_c/W roughly proportional to $1/S$, and the subshear subset shows a hint of a similar

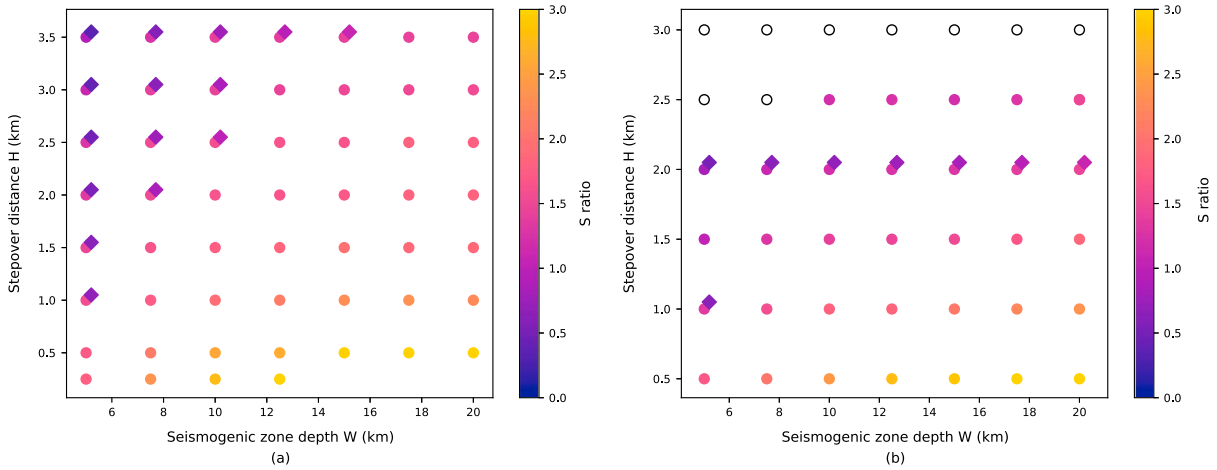

Figure 2. Critical values of the ratio of strength excess to stress drop, S, that allow ruptures to jump (a) compressional and (b) dilational step overs with different seismogenic depth W and step over distance H. Each symbol is the result of a suite of simulations with fixed H and W, but varying S until the maximum S value required for step over jump is found. This critical S value is reported by colors. Two different symbols indicate the rupture speed regime on the first fault: sub-Rayleigh (circles) or supershear (diamonds). Open circles are cases in which only supershear ruptures can jump through the step over; we did not determine the critical S for those cases.

trend at the lowest S values. The boundary between the $1/S^2$ and $1/S$ regimes is close to $S = 1.5$ and $H_c/W = 0.2$. In dilational step overs, the $H_c/W \propto 1/S^2$ regime is also very clear, even within the supershear subset, but not the $1/S$ regime. There are fewer cases in our dilational step over simulations where rupture breaches a step over wider than 0.2 W, so we cannot discard that the inverse linear regime exists outside the parameter ranges we explored. Also in dilational step overs, for a given S value sub-Rayleigh ruptures have larger H_c than supershear ruptures. The simulation results at small H_c/W or large S in both compressional and dilational step overs are adequately represented by the relation $H_c/W = 0.3/S^2$ (dashed lines in Figure 4). There is a slightly larger H_c/W on compressional step overs than on dilational ones, which is consistent with previous findings (Hu et al., 2016).

3.2. Effect of L_c on Critical Step Over Distance and Rupture Speed

The ratio L_c/W modulates the relation between H_c/W and S such that for a given S, larger L_c/W gives smaller H_c/W (Figure 4). The mechanism underlying this observation is that, because the process zone scale L_c is also related to a critical nucleation size (Ampuero et al., 2002; Uenishi & Rice, 2003), a smaller L_c/W facilitates rupture nucleation on the secondary fault.

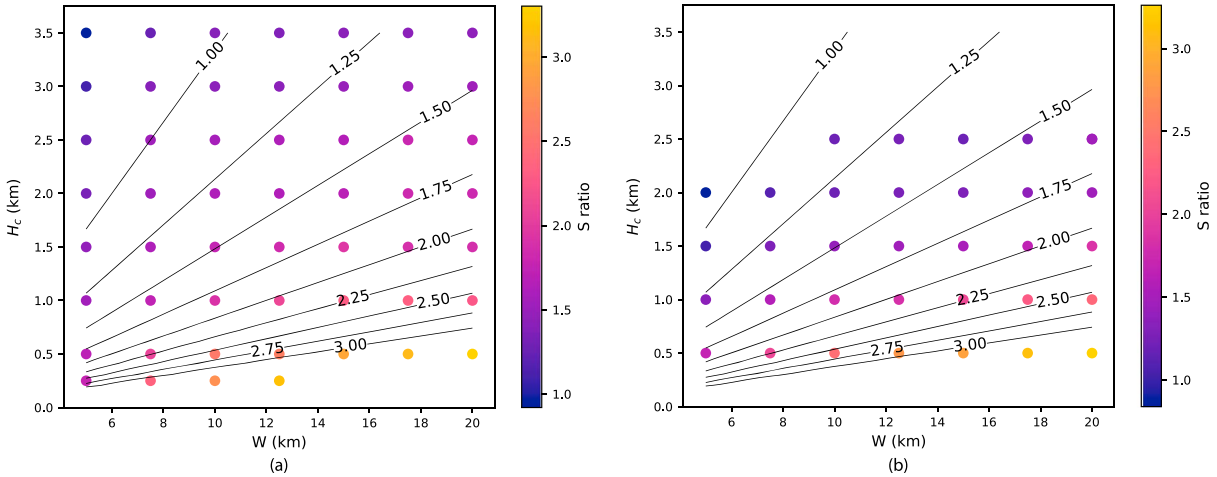

Figure 3. Critical step over distance H_c for sub-Rayleigh ruptures as a function of seismogenic depth W and strength excess ratio S for (a) compressional and (b) dilational step overs. The solid lines are not contours generated from simulation data but the contours of critical S predicted by a relation $H_c/W = 0.3/S^2$ inspired by our near-field theory and constrained by our simulation data. They serve as a visual guide here. The contours of $S_c(W, H)$ are roughly linear, pointing to a relation of the form $H/W \approx f(S_c)$.

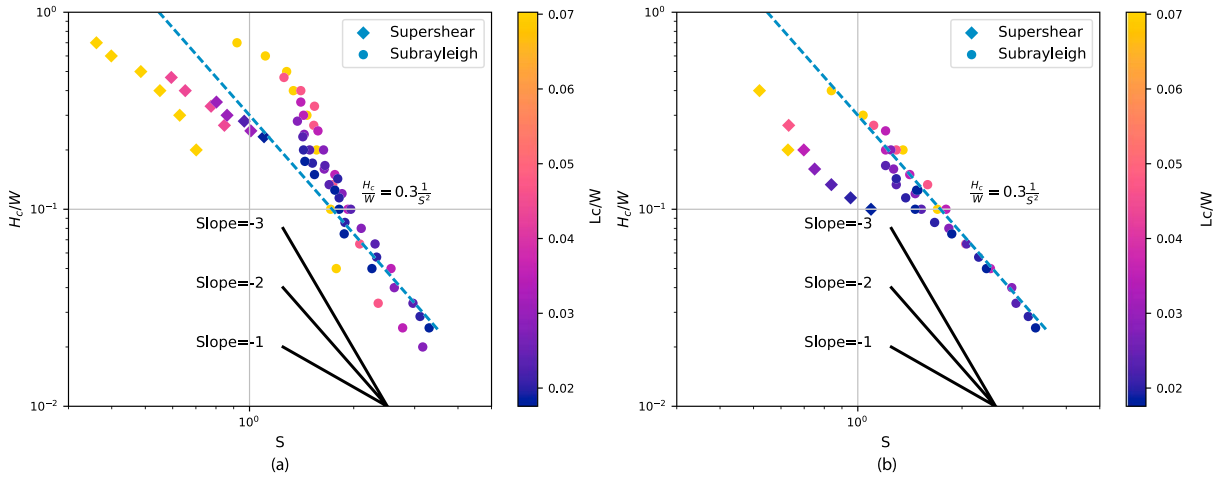

Figure 4. Relation between critical step over distance normalized by seismogenic depth, H_c/W, and strength excess S in (a) compressional and (b) dilational step overs. Simulations span a range of normalized nucleation sizes L_c/W (indicated by colors). Cases with subshear and supershear ruptures on the second fault are distinguished by symbols (see legend). For compressional step overs, the simulation results are consistent with an inverse quadratic relation $H_c/W \propto 1/S^2$ at large $S > 2$ and an inverse linear relation $H_c/W \propto 1/S$ at small $S < 1.5$. The linear regime has two branches corresponding to sub-Rayleigh and supershear ruptures on the second fault. For dilational step overs, the results are consistent with the quadratic relation and also display sub-Rayleigh and supershear branches. In both compressional and dilational step overs, sub-Rayleigh ruptures have larger H_c than supershear ruptures at given S. Small values of L_c/W favor supershear. For a given S value, faults with smaller L_c/W can jump wider step overs.

Apart from a nucleation effect, L_c also affects H_c by affecting the terminal rupture speed on the primary fault. The terminal speed of sub-Rayleigh ruptures on the primary fault depends on Lc/W and S. More specifically, it depends on the ratio of fracture energy $G_c = \frac{1}{2}\sigma_0(\mu_s - \mu_d)D_c$ to static energy release rate $G_0 \approx \frac{W\Delta(\tau_0 - \mu_d\sigma_0)}{2\mu}$, which is proportional to $(1+S)^2 L_c/W$. The smaller the ratio G_c/G_0 is, the larger the terminal rupture speed can be. In Figure 5 we show that the relation between V_r and G_c/G_0 obtained in our simulations is consistent with the theoretical expectation from fracture dynamics (Weng & Yang, 2017).

A more prominent effect of L_c on step over jumps is related to its effect on supershear transitions. The critical S ratio necessary for supershear transition increases as W/L_c increases, consistently with results of previous 3-D studies (Dunham, 2007; Madariaga & Olsen, 2000). Previous numerical simulations (Hu et al., 2016; Lozos et al., 2014) have shown that supershear ruptures can breach a wider step over than sub-Rayleigh ruptures. In particular, when the S ratio decreases to around 0.45, a step over wider than 10 km can be breached by ruptures that have undergone supershear transition assisted by free-surface effects (Hu et al., 2016). On the contrary, in our simulations with free-surface effect suppressed by a shallow layer of negative stress drop, supershear ruptures have shorter H_c than sub-Rayleigh ruptures at given S (Figure 4). We observed that during supershear transition, the rupture front splits into a supershear rupture front and a sub-Rayleigh rupture front following the Burridge-Andrews mechanism (Andrews, 1976). These two fronts are weaker than the original sub-Rayleigh front, hence, less efficient at inducing step over jumps (Figure 6). For most values of H, we find two critical S ratios for step over jump, a larger S_c for sub-Rayleigh ruptures and a smaller one for supershear ruptures. However, there are cases in the dilational step overs where the step over jump happens only when rupture on the first fault is supershear. In these cases, there is only one critical S ratio, the one corresponding to supershear ruptures (open circles in Figure 2).

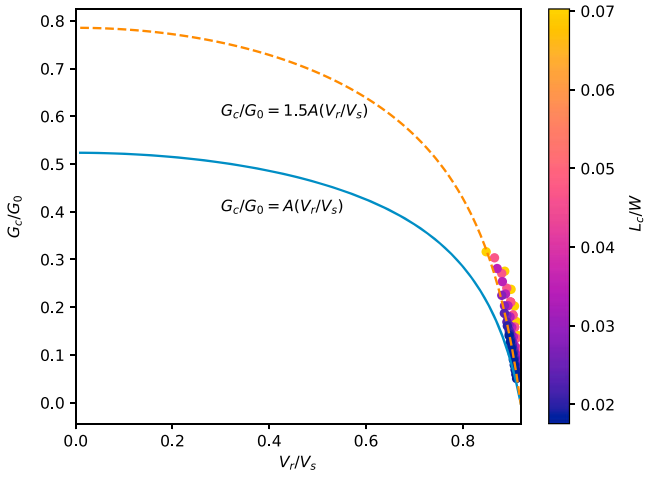

Figure 5. Final rupture speed on the first fault as a function of the ratio between fracture energy G_c and static energy release rate G_0. Rupture speed V_r is normalized by shear wave speed V_S. The blue solid line is the theoretical curve for 2-D mode II cracks with constant rupture speed. A constant factor of 1.5 is introduced to account for 3-D effects, such as curvature of the rupture front.

3.3. Effect of Dynamic Stresses

In principle, both static and dynamic stress transfer from the primary rupture to the secondary fault can contribute to step over jumps. However, 2-D simulations by Oglesby (2008) indicate that dynamic stresses, especially high-frequency stress peaks, are the dominant factor controlling the step

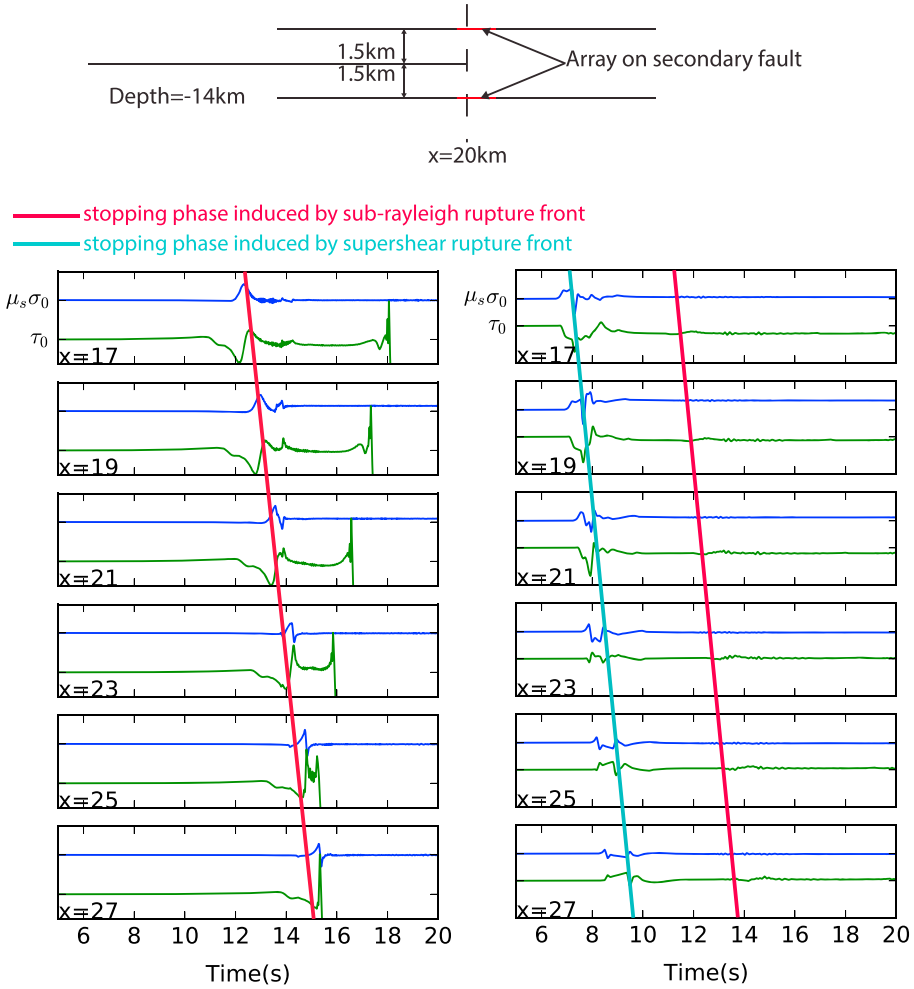

Figure 6. Comparison of dynamic stresses between (left) a sub-Rayleigh rupture and (right) a supershear rupture. (a) Map view of the two examples. Both have the same fault system geometry but different S ratio ($S = 1.27$ for the sub-Rayleigh case and $S = 0.64$ for the supershear case). An array of receivers (red) is placed along the second fault near the end point of the first fault, between $x = 17$ km and 27 km and at a depth of 14 km. (b) Transient shear stress $\tau(t)$ (solid green) and static strength $\mu_s\sigma(t)$ (blue) on the second fault of the sub-Rayleigh case (Figure 6, left) and supershear case (Figure 6, right). Each panel corresponds to a different location along the second fault (x position indicated by label). Stopping phases generated by sub-Rayleigh and supershear fronts are indicated by red and yellow lines, respectively. The supershear rupture did not breach the step over because splitting of the rupture front weakens the peak amplitude of the stopping phase.

over jump behavior. He observed that the critical step over distance depends on how sharp the initial stresses taper at the end of the primary fault, which determines the abruptness of rupture arrest and consequently the amplitude of stopping phases. In 3-D, this effect of stopping phases can be more complicated because the shape of the rupture front can vary depending on S, W, and nucleation processes, generating multiple high-frequency radiation phases when rupture fronts hit the boundary of the seismogenic region. The analysis of the effect of stopping phases in 3-D is made more tractable here by forcing the rupture fronts to be straight, reaching the lateral end of the primary fault almost simultaneously at all depths (section 2). As will be discussed in section 5.5, the straight rupture front assumption will generate an upper bound estimation on H_c due to the constructive interference of the stopping phases.

To demonstrate the predominance of dynamic stresses over static stresses, we show that dynamic stresses are much larger than static stresses in our long rupture models, in which the terminal rupture speed on the first fault is usually close to the Rayleigh wave speed. We select a pair of compressional and dilational step over simulations with the following parameter settings: $S = 1.27$, $H = 1.5$ km, and $W = 15$ km (Figure 7). Static stress analysis would suggest that a dilational step over is easier to breach, because the second fault

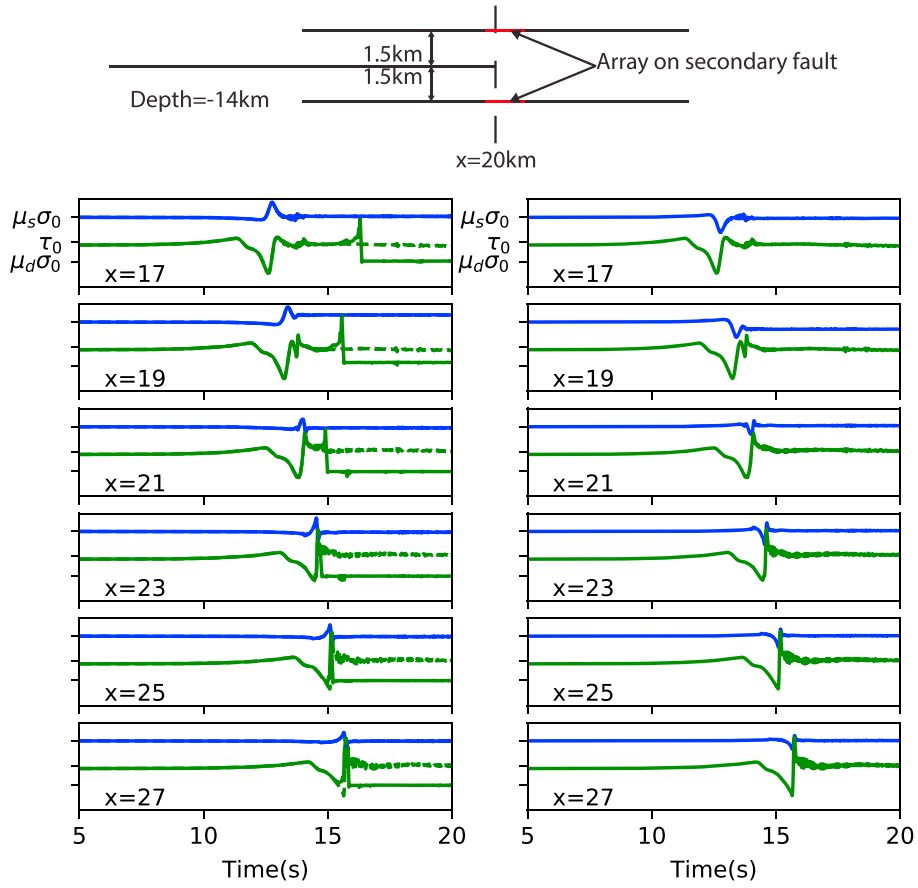

Figure 7. Comparison of dynamic stresses between (left) compressional step over and (right) dilational step over. (a) Map view of the two examples. An array of receivers (red) is placed along the second fault near the end point of the first fault, between $x = 17$ km and 27 km and at a depth of 14 km. (b) Transient shear stress $\tau(t)$ (solid green) and static strength $\mu_s\sigma(t)$ (blue) on the second fault of the compressional step over (Figure 7, left) and dilational step over (Figure 7, right). Each panel corresponds to a different location along the second fault (x position indicated by label). Dashed green curves are shear stresses computed in separate simulations assuming the secondary fault remains locked.

is unclamped (subjected to normal stress reduction) by rupture of the primary fault. However, when we consider the dynamic stresses, results are much more complex. In the compressional step over, static normal stress increases in the second fault but a high-frequency peak in dynamic stress brings it to failure. In the dilational step over example, the static normal stress on the second fault decreases, lowering its strength and thus favoring the step over jump, but the high-frequency dynamic stress peak is not sufficient to bring the fault to failure. In both cases, static stresses alone are not sufficient to breach the step over because of their relatively small amplitude compared with dynamic stresses. A slightly larger compressional step over jump than a dilational one is also observed in most of the examples presented by Hu et al. (2016) and in some of the cases in Lozos et al. (2014) and Ryan and Oglesby (2014), especially in the sub-Rayleigh rupture cases. This implies that the step over distance H_c can be underestimated if only static stress are considered, especially for a compressional step over. Moreover, dynamic Coulomb stresses carried by stopping phases have a different angular pattern than static Coulomb stresses. This pattern is determined by rupture speed and will be discussed in section 4 and Appendix B.

4. Theoretical Relation Between H_c/W and S

The theoretical relation between H_c/W and S cannot be derived analytically in 3-D dynamic rupture problems. However, asymptotic 2-D analysis provides a good approximation to the problem. When a straight rupture front hits the lateral edge of the seismogenic zone producing a line source of length W, the stopping phase it radiates can be approximated as a cylindrical wave in the near field $(0.01 < r/W < 0.1)$, whose amplitude

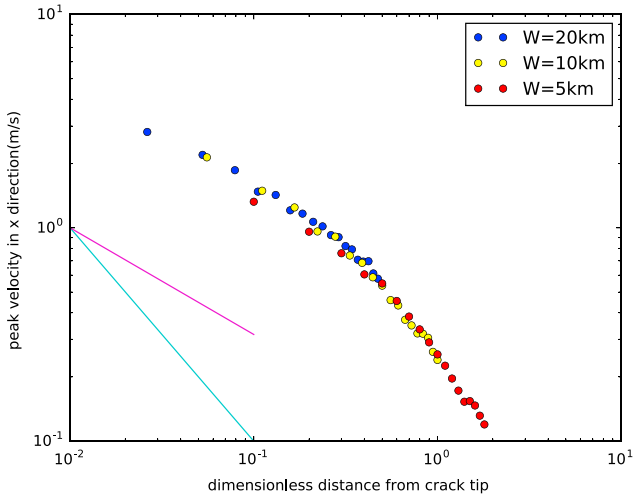

Figure 8. Peak ground velocity in the x direction at 90° azimuth from the end of the first fault, as a function of distance to the end of the first fault normalized by seismogenic depth. Three cases with different seismogenic depth W are considered (see legend).

decays as $\frac{1}{\sqrt{r}}$, and as a spherical wave in the far field ($r/W > 1$), decaying as $\frac{1}{r}$ (Figure 8). Relations between the wave amplitude in these two distance ranges, fault geometry, and dynamic rupture properties are derived in Appendix A. The relations show that the maximum distance at which the Coulomb failure threshold can be reached is proportional to W/S^2 in the near field and proportional to W/S in the far field. This asymptotic analysis of maximum Coulomb failure distance under cylindrical and spherical wave approximations roughly explains what we have observed in the simulations: $H_c/W \propto 1/S^2$ when $H_c/W < 0.1$ (near field) and $H_c/W \propto 1/S$ when $H_c/W > 0.2$ (far field).

The previous analysis of peak dynamic stresses provides a necessary condition for step over jump to happen. Lozos et al. (2014) found qualitatively in 2-D simulations an inverse relation between H_c and the critical slip-weakening distance D_c which is proportional to critical nucleation size. Treating the step over jump problem as a static stress-triggering problem, they proposed that Coulomb failure has to be reached within an area larger than the critical nucleation size on the secondary fault to successfully initiate rupture. Here we further investigate the problem by analysis of the nucleation criterion for 3-D ruptures. The stopping phase of the primary rupture induces a stress pulse traveling at S wave speed on the secondary fault. This pulse has a large aspect ratio, it extends vertically across the whole seismogenic depth but has a short width in the along-strike direction. Galis et al. (2017) found that if the nucleation zone has an aspect ratio greater than 10, spontaneous runaway rupture happens only if its shortest edge length exceeds a critical nucleation size. If $S \leq 3$, this critical nucleation size is independent of S and is equal to the critical nucleation length by Uenishi and Rice (2003), which is close to L_c. If $S > 3$ the nucleation condition does not depend on the aspect ratio, it is equivalent to a critical nucleation area rather than a critical length. However, the very low initial stress when $S > 3$ corresponds to cases where $H_c < 0.03W$ in our simulations. Such small step overs are usually ignored in fault trace mapping and hazard analysis due to the higher likelihood of connection at depth (Graymer et al., 2007) promoting through-going rupture. Thus, for cases of interest, the critical nucleation size L_c of Uenishi and Rice (2003) is an appropriate criterion. Therefore, increasing L_c tends to decrease H_c (Figure 4 color coded by L_c/W). This effect is weak when L_c/W is small. Our previous analysis based on the maximum distance for Coulomb failure to occur hence provides an upper bound on H_c.

5. Discussions

5.1. Comparison to Empirical Observations of H_c

From the analysis of simulation results, we find that the critical step over distance H_c depends primarily on seismogenic width W and strength excess ratio S. In addition, it is slightly modulated by the nucleation size L_c, which is explained by the effect of nucleation on the secondary fault by dynamic stresses carried by stopping phases.

Our modeling results are in first-order agreement with empirical estimates of critical step over distance (Biasi & Wesnousky, 2016; Wesnousky, 2006; Wesnousky & Biasi, 2011). The ratio of shear stress to effective normal stress on the San Andreas fault and other major interplate faults has been inferred to be around 0.2 to 0.3 (Noda et al., 2009), which indicates an S ratio to be greater than 1.5 considering a dynamic friction coefficient of 0.1 and a static friction coefficient of 0.6. When $S > 1.5$, our simulation results for both compressional and dilational step overs are well represented by $H_c/W \approx 0.3/S^2$, and hence, $H_c/W < 0.2$. For a typical $W = 15$ km for continental strike-slip faults we expect $H_c < 3$ km, which agrees with previous observations (Wesnousky, 2006) and numerical simulations (Harris & Day, 1999). The above arguments demonstrate that our new model is consistent with the previous "5 km recipe" when applied to typical continental interplate strike-slip faults.

However, our results indicate that empirical criteria for step over jumps may not be readily applied to faults with different W and S under different tectonic settings, such as oceanic and intraplate strike-slip earthquakes. Our theoretical results provide a more accurate estimate of H_c for given S and W. For a specific region, a range of S values can be constrained by information on regional stresses and fault geometry. The stress state of a fault can be estimated by projecting the regional stress tensor onto the fault plane. The seismogenic depth W can

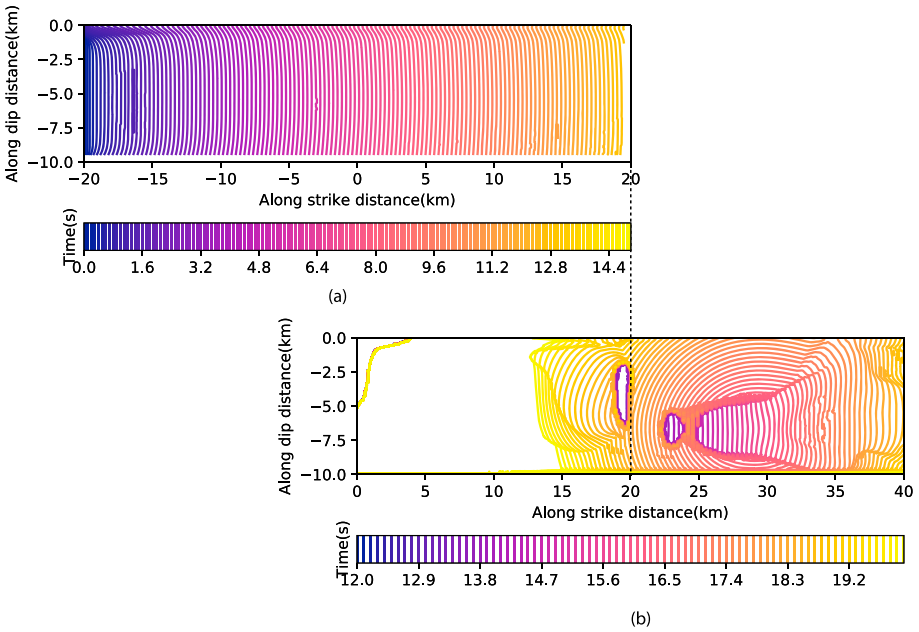

Figure 9. Dilational step over jump with three nucleation attempts. Successful nucleation in the forward direction with respect to the primary fault's end point. Seismogenic depth is $W = 10$ km. Rupture time contours on (top) primary fault and (bottom) secondary fault. The fault overlap section is $0 < x < 20$ km.

be estimated by the termination depth of background seismicity or by geodetic inversion of locking depth. The nucleation size L_c is a more uncertain parameter, which may be inferred from seismological observations of large earthquakes (Fukuyama et al., 2003; Mikumo et al., 2003), but has only a second-order effect on H_c.

Additional support for the major effect of seismogenic depth on critical step over distance is provided by the compilation of empirical observations by Biasi and Wesnousky (2016). Their Figure 9 shows that longer ruptures with similar rupture depth extent are not necessarily stopped by wider step overs. This is consistent with our theoretical arguments in which the amplitude and reach of stresses near the primary rupture tip depend on rupture width but not on rupture length.

5.2. Effect of a Thick Seismogenic Layer

One important factor that challenges the "5 km criterion" is the dependence of H_c on the thickness of the seismogenic layer, W. There are several reasons for variability of seismogenic thickness. The first controlling factor is the geothermal gradient, which controls the brittle to ductile transition of the crust and the deep seismic to aseismic transition of faults. Cooling of an old oceanic crust increases this transition depth and makes the seismogenic layer thicker, which is consistent with a large H_c in the 2012 Indian Ocean earthquake (Meng et al., 2012). The Indian Ocean earthquake has an extraordinary penetration depth of 50 km (Yue et al., 2012) which is 2–3 times the depth of an average continental strike-slip earthquake. So we expect the maximum step over width to be around 10–15 km considering the same S ratio. Moreover, the Indian Ocean earthquake is reported to have larger stress drop (Meng et al., 2012) indicating a smaller S ratio, which makes the observed 20 km step over jump (Meng et al., 2012) a possible scenario. Subduction of an oceanic crust greatly decreases temperature around it, which may deepen the brittle-ductile transition on crustal faults in the overriding plate. This effect has been proposed to explain a rupture depth of 25 km in the 2016 M_w7.8 Kaikoura earthquake inferred from geodetic data (Hamling et al., 2017). For the same thermal reason, we expect intraplate earthquakes to have a thicker seismogenic layer (Copley et al., 2014) and hence a larger H_c than interplate earthquakes.

Dynamic processes that promote large rupture width can favor wider step over jumps. Ruptures can penetrate deeper into the velocity strengthening region where ruptures cannot nucleate spontaneously. Our theory actually relates the critical step over distance to rupture width, more fundamentally than to seismogenic width. Hence, larger step over distances are expected for large earthquake ruptures that penetrate below the seismogenic depth, for instance due to thermal weakening processes (Jiang & Lapusta, 2016).

Our results on strike-slip faults have implications also for other faulting types. To apply our model to dip-slip faults, we need to replace the Mode II stress intensity factor with the Mode III one, which involves a factor of order 1 that depends on Poisson's ratio. In dip-slip faults, the seismogenic width is larger, $W = h/\sin(\alpha)$ where h is the seismogenic depth and α the dip angle. We hence expect H_c to be larger for faults with shallower dip angle α. In addition, the step over distance conventionally defined in map view is larger than the fault distance defined here in the normal direction to the fault plane. Biasi and Wesnousky (2016) found a larger critical step over distance in dip-slip faults, which can be around 12 km.

Relations between fault system geometry and seismogenic depth may complicate the relation between H_c and W. Zuza et al. (2017) found that the spacing between strike-slip faults is also proportional to W. This means that although H_c is larger in areas with thicker seismogenic layer, the probability of a fault step over jump is not necessarily larger because of the sparsity of closely spaced secondary segments.

5.3. Step Over Jumps With Lower Initial Stresses

Our model indicates that ruptures have trouble breaching step overs at low background shear stress (large S ratio yields small H_c/W). On natural faults, we expect $S \gg 1$ to be typical because stress drop estimates are of a few MPa on average and strength drop can be several 10 MPa in the absence of excessive fault zone fluid overpressure. Faults operating at low background stress may have to breach step overs by localizing slip into a more connected fault system (with narrower step overs) (Cooke, 1997; Myers & Aydin, 2004).

In addition to a thicker seismogenic layer (Copley et al., 2014), intraplate earthquakes have average stress drop significantly larger than interplate earthquakes (Allmann & Shearer, 2009; Scholz et al., 1986). Moreover, Kato (2009) suggests that, in contrast to interplate faults, the loading of intraplate faults is dominated by regional plate stressing rather than by aseismic slip in deeper extensions of the fault; hence, the loading of the seismogenic zone tends to be more spatially uniform than on interplate faults. These arguments imply that intraplate faults can operate at overall smaller S ratio than interplate faults, thus allowing for wider step over jumps during earthquakes.

The possibility of step over jumps can be affected by relations between seismogenic depth and the long-term average stress at which a fault operates. In earthquake cycle models of faults loaded by deep creep (Kato, 2012), it is found that as W increases the average stress decreases. Fracture mechanics analysis of this problem leads to a relation that can be formulated as $S+1 \approx \sqrt{W/L_c}$. Together with the relation $H_c/W \propto 1/S^2$ for large S we obtain $H_c \propto L_c$. For small S this model requires $W \approx L_c$ and, considering the relation $H_c/W \propto 1/S$, we obtain $H_c \propto L_c/S$. Hence, the aforementioned class of earthquake cycle models predicts a closer relation between critical step over distance and nucleation size than suggested by our single-earthquake dynamic rupture models.

5.4. A Procedure to Assess the Potential for Step Over Jumps

While our new model incorporates parameters such as W, S, and L_c, it is based on simplifying assumptions that may not be appropriate for all step over problems. For example, we assume the fault strands to be parallel, which is not always the case. As described in Poliakov et al. (2002), the stress field near a propagating mode II rupture promotes secondary ruptures at an angle with the primary fault that depends on the background stress tensor and on rupture speed. Parsons et al. (2012) proposed to estimate the probability of multisegment earthquakes by calculating the static Coulomb stress perturbation induced by one segment on all the surrounding segments. This method neglects dynamic stresses and can lead to substantial underestimation of jumping probability, as shown in section 3.3. We propose the following procedure to assess the potential for a step over jump in a specific case scenario:

1. Run a dynamic rupture simulation on the primary fault.
2. Record the dynamic stress on all secondary faults.
3. Determine if failure is reached over a contiguous zone larger than nucleation size, for given set of initial stresses.

Comparing with the alternative approach of running a dynamic model of the whole specific step over system, our proposed method is more computationally efficient. A conservative estimate is obtained by assuming a very small nucleation size. In step 3, the initial stresses on the secondary faults can be varied over a range constrained by independent considerations, without the need to repeat step 1.

5.5. Potential Limitations

Here we summarize the main limitations of our model and suggest potential improvements or clarify their effects on the estimations of H_c.

We assumed that the initial fault stress results from a homogeneous regional stress field. In reality, fault stresses can be heterogeneous at a step over due to stress concentrations caused by past earthquakes near fault tips. Others have considered different uniform stresses on the two fault segments (Harris & Day, 1999). Revisiting our derivation assuming the stress states on the two faults are different, we find that our H_c prediction equation remains the same after simply replacing S with the ratio S' between the strength excess of the second fault and the stress drop of the first fault. Due to residual stresses left by previous ruptures, S' can be significantly smaller near the step over than our previous estimate of $S > 1$. This allows for larger H_c and reconciles our simulation results with typical observed step over jumps in the kilometer range even when S is high far from the step over. The role of stress heterogeneity on step over jumps can also be addressed through earthquake cycle modeling (Duan & Oglesby, 2006; Shaw & Dieterich, 2007; Yıkılmaz et al., 2015). The fundamental results assuming homogeneous initial stress presented here can help understand the outcomes of such more complete models. For example, we expect initial shear stress to be mostly concentrated near the deep edge of the seismogenic zone due to creep on the deeper portion of the fault (see, e.g., Figure 1 of Kato, 2012). If this stress concentration is substantial, we should observe a tendency for ruptures on secondary faults to initiate in the deepest part of the seismogenic zone. However, the coarse resolution and small number of finite fault inversion results of earthquakes with step over jumps (Field et al., 2014; Hamling et al., 2017; Wald & Heaton, 1994; Yue et al., 2012) do not allow to determine if such a tendency occurs in nature.

We assumed a rectangular rupture area and a vertical rupture front. In reality, rupture area and rupture front can have complicated geometries due to fault geometry as well as stress and frictional heterogeneities, which can generate multiple strong phases. In our model, the rupture front forms a perfect line source and is a worst-case scenario because it generates the strongest constructive interference. Our simulation results thus serve as an upper limit estimation of the amplitude of stopping phase radiation.

We assume rupture termination to be very sharp, as if the rupture encountered a steep increase of fracture energy or a sharp decrease in shear stress. In reality, rupture arrest can be gradual, for instance, if rupture is stopped by an area of smoothly decreasing initial stress (Oglesby, 2008), which leads to weaker stress concentration and stopping phases and hence less efficient step over jumps. In these regard, our model provides an upper bound on H_c, which is useful for a conservative hazard analysis.

Step over jumps can be facilitated by structural features such as intermediate fault segments (Lozos et al., 2015) or linking faults (Oglesby, 2005). An important case is a flower structure, in which two fault segments that are separate at the surface merge into a single fault at some depth. In this case, dynamic rupture simulations by Aochi (2003) showed that ruptures break through the step over by taking advantage of the deep linkage, regardless of how wide the gap is at the surface, unless the deep rupture pathway is too narrow due to a linkage depth too close to the bottom of the seismogenic zone. The step over distance at the surface is proportional to the linkage depth if the average dip angle of the fault branches is controlled by the internal frictional angle of the crust (Di Bucci et al., 2006; Naylor et al., 1986). Thus, flower structures could also lead to critical step over distances H_c proportional to W. Distinguishing between the deeply linked faults interpretation and the parallel faults interpretation of the relation $H_c \propto W$ needs further investigation of the geometry of active faults at depth. Sometimes the evidence is not sufficient to determine if a step over had a linking fault with significant slip over a significant depth range that clearly contributed to the (apparent) step over jump. In some cases a linking fault with little slip, or too shallow slip, may just be a by-product of the larger-scale rupture across the step over without contributing much to it. The theory we developed provides physical bounds on what is possible without linking faults, and this may assist in the interpretation and discussion of specific cases. For example, applying our theory to a particular (hypothetical) example in which surface rupture on a linking fault is documented, one may be able to argue that, given the background stress, stress drop, seismogenic depth and step over distance, in principle, the rupture could have jumped the step over even without a linking fault. In such an example, the theoretical argument can motivate further study of the amount and depth extent of slip on the linking fault in order to assess to what extent it contributed to the rupture across the step over.

We assume that both fault segments are embedded in a homogeneous elastic half-space. However, most fault zones will include a low-velocity layer surrounding the fault plane (Finzi & Langer, 2012a, 2012b; Huang & Ampero, 2011; Lewis & Ben-Zion, 2010,). The elastic modulus of this layer adjacent to the primary fault can be smaller than host rock and also different from the elastic modulus of the layer adjacent to the secondary fault. The gradation in the elastic properties in the overlapping region may contribute to the complexity of the radiated field through multiple reflections and transmissions (Ben-Zion et al., 2003; Huang et al., 2014). For certain frequencies, this may lead to amplification of the dynamic displacement and may affect the rupture trigger ability on the secondary fault.

We assumed a linear slip-weakening friction law, that is, fault strength decreases linearly with accumulated slip. A nonlinear slip-weakening law with steeper weakening at small slip facilitates nucleation (Dunham, 2007) and hence can increase H_c. As is found by Ryan and Oglesby (2014) in their 2-D step over simulations, the functional form of a frictional law has only a second-order effect on a step over problem given constant fracture energy. We thus expect our scaling relation derived from slip-weakening friction law to hold for rate-and-state friction law.

Ruptures propagating on rough faults decelerate and accelerate nonuniformly, leading to enhanced seismic radiation (Shi & Day, 2013). Also, a rupture on a nonplanar fault may stop abruptly before reaching the end of the fault due to strong variations in the fault strike or stress heterogeneity. This would also be a source of stopping phases and strong radiation (Madariaga et al., 2006). The former may promote jumping large step overs by enhancing the high-frequency component of the wave field. The latter may be important to investigate in future studies for its implication on earthquake triggering or delayed jumping across fault segments.

Ample evidence from laboratory and numerical studies points to the relevance of enhanced dynamic weakening during fast rupture propagation, while rupture nucleation is controlled by rate-and-state frictional behavior (Noda & Lapusta, 2013; Rice, 2006). As a consequence, nucleation sizes on natural faults can be orders of magnitude smaller than what is assumed in the present study. However, as the critical nucleation size decreases toward 0, we expect H_c to increase and converge to an upper bound value controlled by stress amplitude rather than nucleation size. This upper bound is given by the theory developed in section 4 and is close to the value obtained in our simulation results.

To simplify the discussion, we focus our attention on cases with $S < 3$, for which the critical nucleation size has a weak dependence on S. For $S > 3$, the critical nucleation size increases rapidly with S, and the critical step over distance could be even smaller than predicted by extrapolating the results presented in Figure 4.

6. Conclusions

The present computational and theoretical study of earthquake rupture on faults with step overs provides fundamental insights on the physical factors, controlling the limits on the step over distance that a rupture can jump. By conducting a systematic set of 3-D dynamic rupture simulations on strike-slip faults with uniform prestress and friction properties, we have established theoretical dependencies of the critical step over jump distance H_c on seismogenic depth W, prestress level S (the ratio of strength excess to stress drop) and critical nucleation size L_c (the ratio of shear modulus to slip-weakening rate). An understanding of the mechanical origins of these dependencies is obtained by analytical arguments based on fracture mechanics. A critical step over jump distance model of the form

$$H_c \propto W/S^n$$

is established where $n = 2$ in the near-field regime when $H_c < 0.2W$ (or $S > 1.5$) and $n = 1$ in the far-field regime when $H_c > 0.2W$ (or $S < 1.5$). Nucleation size has a second-order effect on critical step over distance; increasing L_c decreases H_c mildly.

We estimate the critical step over distance to be a fraction of the seismogenic depth. This theoretical estimate is of the same order of magnitude as the maximum step over distances derived empirically for continental strike-slip faults. Our model, in particular, predicts that earthquakes with exceptionally large rupture depth extension can breach proportionally wide step overs. This prediction is consistent with observations of earthquakes in regions of thick oceanic lithosphere for which ruptures breaching step overs wider than 10 km have been reported, such as the 2012 M_w8.6 Indian Ocean earthquake (Meng et al., 2012). Our results also suggest that the maximum step over distance widely used in hazard analysis may not be conservative enough for faults that operate at relatively high average stress and have thicker seismogenic zone, for instance, intraplate faults.

Appendix A: Critical Step Over Distance in the Near-Field and Far-Field Regimes

We develop an upper bound on H_c based on asymptotic stress analysis near a singular crack tip, ignoring the role of cohesive zone size L_c. The stress field at close distance r and azimuth θ (counterclockwise, relative to the rupture direction) from a running crack tip is

$$\sigma_{ij}(r,\theta) \approx \sigma_{0,ij}(r,\theta) + \frac{K_d \Sigma_{d,ij}(\theta)}{\sqrt{r}} \tag{A1}$$

where K_d is the dynamic stress intensity factor, which is a function of rupture speed, and $\Sigma_{d,ij}(\theta)$ is an angular pattern. Theory (Madariaga, 1977, 1983) and numerical simulations (Madariaga et al., 2006) show that this sudden change of stress intensity factor causes radiation of strong high-frequency phases. If arrest is simultaneous along the terminal edge of the first fault, the stopping phase is radiated by a line source of finite length W. Hence, in the near field ($r/W \ll 1$) the stopping phase is approximately a cylindrical wave, but in the far field ($r/W \gg 1$) it is a spherical wave. This creates two different amplitude-distance decay regimes: the stopping phase amplitude is proportional to $1/\sqrt{r}$ when $r/W \ll 1$ and to $1/r$ when $r/W \gg 1$. The stress field near the crack tip (at distance r and azimuth θ from the first fault tip) when there is a sudden arrest of the rupture can be decomposed into three parts: (1) the background homogeneous stress $\sigma_{0,ij}$; (2) the static stress field $\sigma_{s,ij}(r,\theta)$ caused by the running rupture right before the rupture arrest $\sigma_{s,ij}(r,\theta) = \frac{K_d \Sigma_{d,ij}(\theta)}{\sqrt{r}}$; and (3) the stopping phase caused by the simultaneous arrest of the rupture along the lateral edge. Only the third part is time dependent, and we refer to Madariaga (1977), equation (36), which is the solution of S wave stopping phase for 2-D in-plane shear rupture. We omit other complicated wave phenomenon while only keeping the S wave part of the stopping phase, which we observed to be the major contributing factor. We compact all the other terms of Madariaga (1977), equation (36), into $\Sigma_{sp,ij}(V_r,\theta)$ while we highlight the dependence of part 3 on K_s and r

$$\sigma_{ij}(r,\theta,t) = \sigma_{0,ij} + \frac{K_d \Sigma_{d,ij}(\theta)}{\sqrt{r}} + \frac{K_s \Sigma_{sp,ij}(V_r,\theta)}{\sqrt{r}} H(t - r/V_s), \tag{A2}$$

and in the far field

$$\sigma_{ij}(r,\theta,t) = \sigma_{0,ij} + \frac{C_s \Pi_{sp,ij}(Vr,\theta)}{r} H(r - t/V_s), \tag{A3}$$

$\Sigma_{sp,ij}(V_r,\theta)$ and $\Pi_{sp,ij}(V_r,\theta)$ are near-field and far-field angular patterns. We have observed the rupture jump to occur after the pass of the stopping phase which means $H(r - t/V_s) = 1$. Since the dynamic wave field is much larger than the static component at large distance, we have omitted the static component in the far field expression. For a 3-D rectangular crack with large aspect ratio ($L/W > 0.25$), K at the short edge is very close to that of a mode II crack in 2-D with length W (Noda & Kihara, 2002): $K_s, K_d \propto \Delta\tau\sqrt{W}$ if $L \gg W$. We define

$$\kappa_{ij}(V_r,\theta) = \frac{K_d \Sigma_{d,ij}(\theta) + K_s \Sigma_{sp,ij}(V_r,\theta)}{\Delta\tau\sqrt{W}} \tag{A4}$$

and

$$\xi_{ij}(Vr,\theta) = \frac{C_s \Pi_{sp,ij}(Vr,\theta)}{W\Delta\tau} \tag{A5}$$

These quantities are dimensionless and have no dependencies on W and S ratio. After inserting these dimensionless quantities, the stress on the second fault is

$$\sigma_{ij}(r,\theta) = \sigma_{0,ij} + \frac{\kappa_{ij}(Vr,\theta)}{\sqrt{r/W}} \tag{A6}$$

in the near field and

$$\sigma_{ij}(r,\theta) = \sigma_{0,ij} + \frac{\xi_{ij}(Vr,\theta)}{r/W} \tag{A7}$$

in the far field. A necessary condition for rupture on the second fault is that the shear stress exceeds the static frictional strength:

$$\tau(r_c,\theta_c) > \mu_s \sigma(r_c,\theta_c) \tag{A8}$$

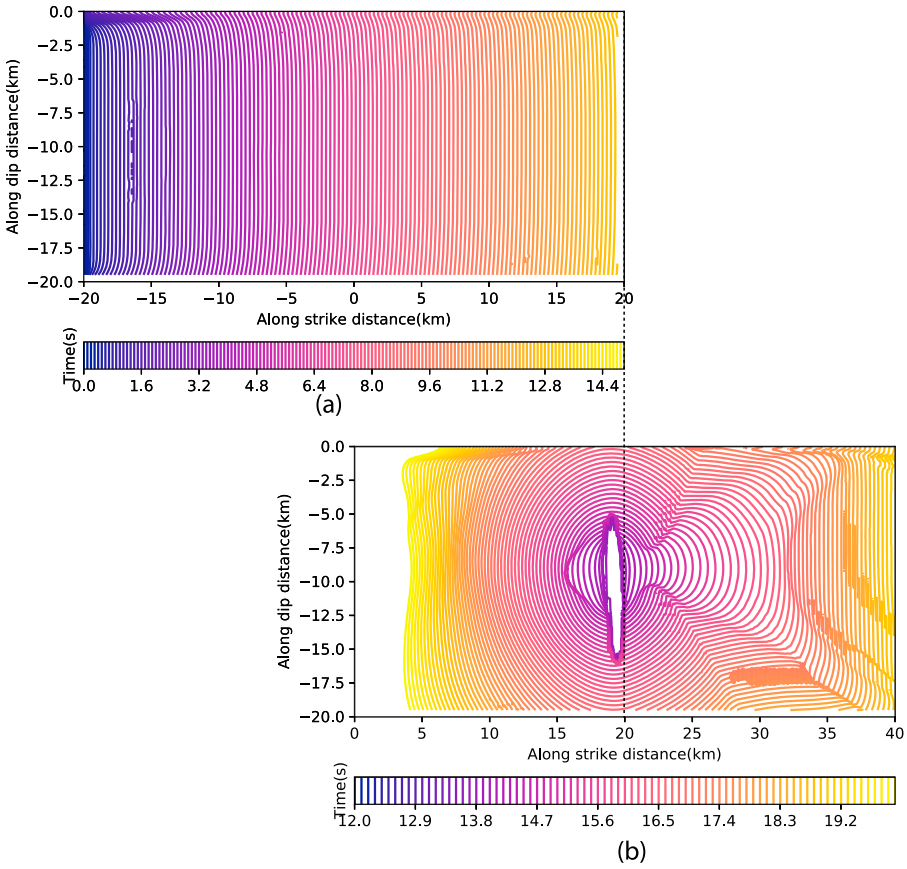

Figure A1. Nucleation in the backward direction for a dilational step over with $W = 20$ km.

where fault shear stress is $\tau = \sigma_{xy}$ and normal stress is $\sigma = \sigma_{yy}$. To satisfy this necessary condition with maximum step over distance

$$H_c = r_c \sin(\theta_c) \tag{A9}$$

we need to find r_c and θ_c that maximize $r_c \sin(\theta_c)$ under the constraint (A8). Solving this optimization problem is difficult if θ_c depends on S. However, we have observed that θ_c is almost constant, with value near 30°, in all our compressional step over simulations. In dilational step overs, for most cases with $W > 10$ km nucleation also occurs at a fixed azimuth of around −120° in the backward direction (Figure A1), which is consistent with previous 2-D simulations (Harris & Day, 1999). There are exceptions when $W < 10$ km in which the backward nucleation fails to develop into a sustained rupture (Figure 9). Assuming a fixed θ_c, the problem is reduced to finding the largest H_c that satisfies the following relations:

$$\tau_0 + \Delta\tau \frac{\kappa_{xy}(V_r, \theta_c)(\sqrt{\sin(\theta_c)})}{\sqrt{H_c/W}} > \mu_s \left(\sigma_0 + \frac{\kappa_{yy}(V_r, \theta_c)\sqrt{\sin(\theta_c)}}{\sqrt{H_c/W}} \right) \tag{A10}$$

in the near field and

$$\tau_0 + \Delta\tau \frac{\xi_{xy}(V_r, \theta_c)\sin(\theta_c)}{H_c/W} > \mu_s \left(\sigma_0 + \frac{\xi_{yy}(V_r, \theta_c)\sin(\theta_c)}{Hc/W} \right) \tag{A11}$$

in the far field. The solution is

$$H_c/W = \frac{(\mu_s \kappa_{yy}(V_r, \theta_c) - \kappa_{xy}(V_r, \theta_c))^2 \sin(\theta_c)}{S^2} \tag{A12}$$

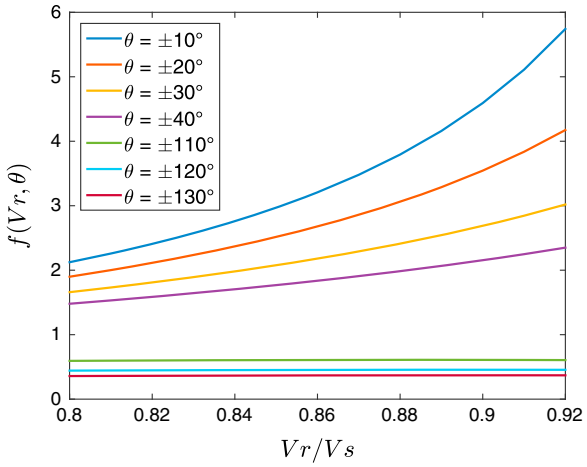

Figure B1. The dependence of angular pattern on rupture speed V_r at different azimuths. The dependence is smooth and weak within the range of the azimuths and speeds we are interested in.

in the near field and

$$H_c/W = \frac{(\mu_s \xi_{yy}(V_r, \theta_c) - \xi_{xy}(V_r, \theta_c))\sin(\theta_c)}{S} \tag{A13}$$

in the far field.

Rupture speed is very similar in all our examples (Figure 5). Within that range, $V_r/V_s > 0.8$, rupture speed does not affect significantly the radiation amplitude in the azimuths we are interested in, as shown in Appendix B. Hence, Hc/W is not significantly affected by Vr.

Appendix B: Effect of V_r on the Amplitude of Stopping Phases

The first motion velocity amplitude of the S wave stopping phase of a Mode II crack is (equation (36) of Madariaga, 1977):

$$\frac{u^s(r,\theta,t)}{\partial t} = \frac{K_0}{\mu} V_r \frac{1}{\sqrt{r}} F_s(V_r,\theta) H(t - r/V_s) \tag{B1}$$

where

$$F_s(V_r,\theta) = \frac{\kappa^3 \cos(2\theta)\cos(\theta/2)}{2(\kappa^2-1)(1 - V_r/V_s \cos\theta)(q_R + \kappa cos\theta) S(\cos\theta/V_s)} \tag{B2}$$

and q_R is the Rayleigh function, which depends on V_r and $\kappa = V_p/V_s$. So

$$u^s_\theta(r,\psi,t) = \frac{K_0}{\mu} V_r \frac{1}{\sqrt{r}} F_s(V_r,\theta) R(t - r/V_s) \tag{B3}$$

where $R(t) = \max(0, t)$ is the ramp function. Then

$$\frac{\partial u^s_\theta}{\partial r} = -\frac{1}{V_s}\frac{\partial u^s_\theta}{\partial t} - \frac{1}{2}\frac{K_0}{\mu} V_r \frac{1}{r^{3/2}} F_s(V_r,\theta) R(t - r/V_s) \tag{B4}$$

$$\frac{\partial u^s_\theta}{\partial \theta} = \frac{K_0}{\mu} V_r \frac{1}{\sqrt{r}} F_s(V_r,\theta) R(t - r/V_s) \tag{B5}$$

At $t = r/V_s$, we have $\frac{\partial u^s_\theta}{\partial t} = -\frac{1}{V_s}\frac{\partial u^s_\theta}{\partial r}$ and $\frac{\partial u^s_\theta}{\partial \theta} = 0$. We convert the strain tensor from cylindrical coordinates to Cartesian coordinates, and by introducing Lame's parameter λ and μ, stress can be calculated as

$$\tau = \sigma_{xy} = \mu \cos(2\theta)\frac{\partial u_\theta}{\partial r} \tag{B6}$$

$$\sigma = \sigma_{yy} = \mu \sin(2\theta)\frac{\partial u_\theta}{\partial r} \tag{B7}$$

The only dependence of $\tau - \mu_s\sigma$ on V_r is in the expression of $\partial u_\theta/\partial r$, via the term

$$f(V_r,\theta) = \frac{V_r/V_s}{(1 - V_r/V_s \cos\theta)(q_R + \cos\theta)} \tag{B8}$$

We plot the function $f(V_r, \theta)$ for a range of rupture speeds representative of our simulations and for a broad range of azimuths. In our simulations, $\theta = 30°$ and $\theta = 120°$ are the angles θ_c at which we observe compressional and dilational step over jumps, respectively (Figure B1).

Acknowledgments
This work was funded by NSF CAREER award EAR-1015698 and by the Southern California Earthquake Center (Contribution 7964), which is funded by National Science Foundation Cooperative Agreement EAR-82081033462 and U.S. Geological Survey Cooperative Agreement G12AC20038. We thank Julian Lozos, an anonymous reviewer and Associate Editor Yoshi Kaneko for their constructive suggestions to improve this manuscript. All data generating figures in this paper are available at https://drive.google.com/open?id=0B-S2bwIdZxdfYkRhTzF4NXdRWWs.

References

Allmann, B. P., & Shearer, P. M. (2009). Global variations of stress drop for moderate to large earthquakes. *Journal of Geophysical Research*, *114*, B01310. https://doi.org/10.1029/2008JB005821

Ampuero, J. P., & Mao, X. (2017). Upper limit on damage zone thickness controlled by seismogenic depth. *Fault Zone Dynamic Processes: Evolution of Fault Properties During Seismic Rupture*, *227*, 243.

Ampuero, J.-P., Vilotte, J.-P., & Sanchez-Sesma, F. J. (2002). Nucleation of rupture under slip dependent friction law: Simple models of fault zone. *Journal of Geophysical Research*, *107*(B12), 2324. https://doi.org/10.1029/2001JB000452

Andrews, D. (1976). Rupture velocity of plane strain shear cracks. *Journal of Geophysical Research*, *81*(32), 5679–5687.

Aochi, H. (2003). The role of fault continuity at depth in numerical simulations of earthquake rupture. *Bulletin of the Earthquake Research Institute University of Tokyo*, *78*, 75–82.

Ben-Zion, Y., Peng, Z., Okaya, D., Seeber, L., Armbruster, J. G., … Aktar, M. (2003). A shallow fault-zone structure illuminated by trapped waves in the Karadere–Duzce branch of the North Anatolian Fault, Western Turkey. *Geophysical Journal International*, *152*(3), 699–717.

Biasi, G. P., & Wesnousky, S. G. (2016). Steps and gaps in ground ruptures: Empirical bounds on rupture propagation. *Bulletin of the Seismological Society of America*, *106*(3), 1110–1124.

Cooke, M. L. (1997). Fracture localization along faults with spatially varying friction. *Journal of Geophysical Research*, *102*(B10), 22,425–22,434. https://doi.org/10.1029/97JB01829

Copley, A., Mitra, S., Sloan, R. A., Gaonkar, S., & Reynolds, K. (2014). Active faulting in apparently stable peninsular India: Rift inversion and a Holocene-age great earthquake on the Tapti Fault. *Journal of Geophysical Research: Solid Earth*, *119*, 6650–6666. https://doi.org/10.1002/2014JB011294

Das, S., & Aki, K. (1977). Fault plane with barriers: A versatile earthquake model. *Journal of Geophysical Research*, *82*(36), 5658–5670.

Day, S. M. (1982). Three-dimensional simulation of spontaneous rupture: The effect of nonuniform prestress. *Bulletin of the Seismological Society of America*, *72*(6A), 1881–1902.

de Joussineau, G., & Aydin, A. (2007). The evolution of the damage zone with fault growth in sandstone and its multiscale characteristics. *Journal of Geophysical Research*, *112*, B12401. https://doi.org/10.1029/2006JB004711

Di Bucci, D., Ravaglia, A., Seno, S., Toscani, G., Fracassi, U., & Valensise, G. (2006). Seismotectonics of the southern Apennines and Adriatic foreland: Insights on active regional E-W shear zones from analogue modeling. *Tectonics*, *25*, TC4015. https://doi.org/10.1029/2005TC001898

Duan, B., & Oglesby, D. D. (2006). Heterogeneous fault stresses from previous earthquakes and the effect on dynamics of parallel strike-slip faults. *Journal Of Geophysical Research*, *111*, B05309. https://doi.org/10.1029/2005JB004138

Dunham, E. M. (2007). Conditions governing the occurrence of supershear ruptures under slip-weakening friction. *Journal of Geophysical Research*, *112*, B07302. https://doi.org/10.1029/2006JB004717

Elliott, A., Dolan, J., & Oglesby, D. (2009). Evidence from coseismic slip gradients for dynamic control on rupture propagation and arrest through stepovers. *Journal of Geophysical Research*, *114*, B02313. https://doi.org/10.1029/2008JB005969

Field, E. H., Arrowsmith, R. J., Biasi, G. P., Bird, P., Dawson, T. E., Felzer, K. R., … Working Group on CA Earthquake Probabilities (2014). Uniform California Earthquake Rupture Forecast, version 3 (UCERF3) the time-independent model. *Bulletin of the Seismological Society of America*, *104*(3), 1122–1180.

Finzi, Y., & Langer, S. (2012a). Damage in step-overs may enable large cascading earthquakes. *Geophysical Research Letters*, *39*, L16303. https://doi.org/10.1029/2012GL052436

Finzi, Y., & Langer, S. (2012b). Predicting rupture arrests, rupture jumps and cascading earthquakes. *Journal of Geophysical Research*, *117*, B12303. https://doi.org/10.1029/2012JB009544

Fukuyama, E., Mikumo, T., & Olsen, K. B. (2003). Estimation of the critical slip-weakening distance: Theoretical background. *Bulletin of the Seismological Society of America*, *93*(4), 1835–1840.

Galis, M., Pelties, C., Kristek, J., Moczo, P., Ampuero, J. P., & Mai, P. M. (2015). On the initiation of sustained slip-weakening ruptures by localized stresses. *Geophysical Journal International*, *200*(2), 890–909.

Galis, M., Ampuero, J.-P., Mai, P. M., & Cappa, F. (2017). Theoretical estimates of magnitudes of earthquakes induced by pore-pressure perturbations with large aspect ratios. In *19th EGU General Assembly, EGU2017, Proceedings from the Lonference held 23-28 April, 2017* (Vol. 19, pp. 6111). Vienna, Austria.

Galvez, P., Ampuero, J.-P., Dalguer, L., Somala, S., & Nissen-Meyer, T. (2014). Dynamic earthquake rupture modelled with an unstructured 3-D spectral element method applied to the 2011 *M*9 Tohoku earthquake. *Geophysical Journal International*, *198*(2), 1222–1240.

Graymer, R., Langenheim, V., Simpson, R., Jachens, R., & Ponce, D. (2007). Relatively simple through-going fault planes at large-earthquake depth may be concealed by the surface complexity of strike-slip faults. *Geological Society, London, Special Publications*, *290*(1), 189–201.

Hamling, I. J., Hreinsdóttir, S., Clark, K., Elliott, J., Liang, C., Fielding, E., … Stirling, M. (2017). Complex multifault rupture during the 2016 M_w 7.8 Kaikōura earthquake, New Zealand. *Science*, *356*(6334), eaam7194.

Harris, R. A., & Day, S. M. (1999). Dynamic 3D simulations of earthquakes on en echelon faults. *Geophysical Research Letters*, *26*(14), 2089–2092.

Harris, R. A., Archuleta, R. J., & Day, S. M. (1991). Fault steps and the dynamic rupture process: 2-D numerical simulations of a spontaneously propagating shear fracture. *Geophysical Research Letters*, *18*(5), 893–896. https://doi.org/10.1029/91GL01061

Herbert, J. W., Cooke, M. L., Oskin, M., & Difo, O. (2014). How much can off-fault deformation contribute to the slip rate discrepancy within the eastern California shear zone? *Geology*, *42*(1), 71–75.

Hu, F., Zhang, Z., & Chen, X. (2016). Investigation of earthquake jump distance for strike-slip step overs based on 3D dynamic rupture simulations in an elastic half-space. *Journal of Geophysical Research: Solid Earth*, *121*, 994–1006. https://doi.org/10.1002/2015jb012696

Huang, Y., & Ampuero, J.-P. (2011). Pulse-like ruptures induced by low-velocity fault zones. *Journal of Geophysical Research*, *116*, B12307. https://doi.org/10.1029/2011JB008684

Huang, Y., Ampuero, J.-P., & Helmberger, D. V. (2014). Earthquake ruptures modulated by waves in damaged fault zones. *Journal of Geophysical Research: Solid Earth*, *119*, 3133–3154. https://doi.org/10.1002/2013JB010724

Ida, Y. (1972). Cohesive force across the tip of a longitudinal-shear crack and Griffith's specific surface energy. *Journal of Geophysical Research*, *77*(20), 3796–3805. https://doi.org/10.1029/JB077i020p03796

Ikari, M. J., Saffer, D. M., & Marone, C. (2009). Frictional and hydrologic properties of clay-rich fault gouge. *Journal of Geophysical Research*, *114*, B05409. https://doi.org/10.1029/2008JB006089

Jiang, J., & Lapusta, N. (2016). Deeper penetration of large earthquakes on seismically quiescent faults. *Science*, *352*(6291), 1293–1297.

Kaneko, Y., Lapusta, N., & Ampuero, J.-P. (2008). Spectral element modeling of spontaneous earthquake rupture on rate and state faults: Effect of velocity-strengthening friction at shallow depths. *Journal of Geophysical Research*, *113*, B09317. https://doi.org/10.1029/2007JB005553

Kato, N. (2009). A possible explanation for difference in stress drop between intraplate and interplate earthquakes. *Geophysical Research Letters*, *36*, L2331. https://doi.org/029/2009GL040985

Kato, N. (2012). Dependence of earthquake stress drop on critical slip-weakening distance. *Journal of Geophysical Research*, *117*, B01301. https://doi.org/10.1029/2011JB008359

Komatitsch, D., & Tromp, J. (1999). Introduction to the spectral element method for three-dimensional seismic wave propagation. *Geophysical Journal International*, *139*(3), 806–822. https://doi.org/10.1046/j.1365-246X.1999. 00967.x

Komatitsch, D., Göddeke, D., Erlebacher, G., & Michéa, D. (2010). Modeling the propagation of elastic waves using spectral elements on a cluster of 192 GPUs. *Computer Science-Research and Development*, *25*(1–2), 75–82.

Lewis, M. A., & Ben-Zion, Y. (2010). Diversity of fault zone damage and trapping structures in the Parkfield section of the San Andreas Fault from comprehensive analysis of near fault seismograms. *Geophysical Journal International*, *183*(3), 1579–1595.

Lozos, J. C., Dieterich, J. H., & Oglesby, D. D. (2014). The effects of d0 on rupture propagation on fault stepovers. *Bulletin of the Seismological Society of America*, *104*, 1947–1953.

Lozos, J. C., Oglesby, D. D., Brune, J. N., & Olsen, K. B. (2015). Rupture propagation and ground motion of strike-slip stepovers with intermediate fault segments. *Bulletin of the Seismological Society of America*, *105*(1), 387–399.

Madariaga, R. (1977). High-frequency radiation from crack (stress drop) models of earthquake faulting. *Geophysical Journal International*, *51*(3), 625–651.

Madariaga, R. (1983). High frequency radiation from dynamic earthquake fault models. *Annales de Geophysique*, *1*, 17–23.

Madariaga, R., & Olsen, K. B. (2000). Criticality of rupture dynamics in 3D. In *Microscopic and macroscopic simulation: Towards predictive modelling of the earthquake process* (pp. 981–2001). Springer.

Madariaga, R., Ampuero, J., & Adda-Bedia, M. (2006). Seismic radiation from simple models of earthquakes. In R. Abercrombie, A. McGarr, G. Di Toro, & H. Kanamori (Eds.), *Earthquakes: Radiated energy and the physics of faulting, Geophysical Monograp Series* (Vol. 170, pp. 223–236). Washington, DC: American Geophysical Union.

Marone, C., & Scholz, C. (1988). The depth of seismic faulting and the upper transition from stable to unstable slip regimes. *Geophysical Research Letters*, *15*(6), 621–624.

Meng, L., Ampuero, J.-P., Stock, J., Duputel, Z., Luo, Y., & Tsai, V. (2012). Earthquake in a maze: Compressiona rupture branching during the 2012 M_W 8.6 Sumatra earthquake. *Science*, *337*(6095), 724–726.

Mikumo, T., Olsen, K. B., Fukuyama, E., & Yagi, Y. (2003). Stress-breakdown time and slip-weakening distance inferred from slip-velocity functions on earthquake faults. *Bulletin of the Seismological Society of America*, *93*(1), 264–282.

Myers, R., & Aydin, A. (2004). The evolution of faults formed by shearing across joint zones in sandstone. *Journal of Structural Geology*, *26*(5), 947–966.

Naylor, M., Mandl, G. t., & Supesteijn, C. (1986). Fault geometries in basement-induced wrench faulting under different initial stress states. *Journal of Structural Geology*, *8*(7), 737–752.

Noda, H., & Lapusta, N. (2013). Stable creeping fault segments can become destructive as a result of dynamic weakening. *Nature*, *493*(7433), 518–521.

Noda, H., Dunham, E. M., & Rice, J. R. (2009). Earthquake ruptures with thermal weakening and the operation of major faults at low overall stress levels. *Journal of Geophysical Research*, *114*, B07302. https://doi.org/10.1029/2008JB006143

Noda, N.-A., & Kihara, T.-A. (2002). Variation of the stress intensity factor along the front of a 3-D rectangular crack subjected to mixed-mode load. *Archive of Applied Mechanics*, *72*(8), 599–614.

Oglesby, D. (2008). Rupture termination and jump on parallel offset faults. *Bulletin of the Seismological Society of America*, *98*(1), 440–447.

Oglesby, D. D. (2005). The dynamics of strike-slip step-overs with linking dip-slip faults. *Bulletin of the Seismological Society of America*, *95*(5), 1604–1622.

Oskin, M. E., Arrowsmith, J. R., Corona, A. H., Elliott, A. J., Fletcher, J. M., Fielding, E. J., … Teran, O. J. (2012). Near-field deformation from the El Mayor–Cucapah earthquake revealed by differential lidar. *Science*, *335*(6069), 702–705.

Palmer, A. C., & Rice, J. (1973). The growth of slip surfaces in the progressive failure of over-consolidated clay. *Proceedings of the Royal Society of London A: Mathematical Physical and Engineering Sciences*, *332*, 527–548. The Royal Society.

Parsons, T., Field, E. H., Page, M. T., & Milner, K. (2012). Possible earthquake rupture connections on mapped California faults ranked by calculated Coulomb linking stresses. *Bulletin of the Seismological Society of America*, *102*(6), 2667–2676.

Poliakov, A. N., Dmowska, R., & Rice, J. R. (2002). Dynamic shear rupture interactions with fault bends and off-axis secondary faulting. *Journal of Geophysical Research*, *107*(B11), 229.

Rice, J. R. (2006). Heating and weakening of faults during earthquake slip. *Journal of Geophysical Research*, *111*, B05311. https://doi.org/10.1029/2005JB004006

Ryan, K. J., & Oglesby, D. D. (2014). Dynamically modeling fault step overs using various friction laws. *Journal of Geophysical Research: Solid Earth*, *119*, 5814–5829. https://doi.org/10.1002/2014JB011151

Scholz, C. H., Aviles, C., & Wesnousky, S. G. (1986). Scaling differences between large interplate and intraplate earthquakes. *Bulletin of the Seismological Society of America*, *76*(1), 65–70.

Shaw, B. E., & Dieterich, J. H. (2007). Probabilities for jumping fault segment stepovers. *Geophysical Research Letters*, *34*, L01307. https://doi.org/10.1029/2006GL027980

Shi, Z., & Day, S. M. (2013). Rupture dynamics and ground motion from 3-D rough-fault simulations. *Journal of Geophysical Research: Solid Earth*, *118*, 1122–1141. https://doi.org/10.1002/jgrb.50094

Sieh, K., Jones, L., Hauksson, E., Hudnut, K., Eberhart-Phillips, D., Heaton, T., … Zachariasen, J. (1993). Near-field investigations of the Landers earthquake sequence, April to July 1992. *Science*, *260*, 171–171.

Uenishi, K., & Rice, J. R. (2003). Universal nucleation length for slip-weakening rupture instability under nonuniform fault loading. *Journal of Geophysical Research*, *108*, 2042. https://doi.org/10.1029/2001JB001681

Wald, D. J., & Heaton, T. H. (1994). Spatial and temporal distribution of slip for the 1992 Landers, California, earthquake. *Bulletin of the Seismological Society of America*, *84*(3), 668–691.

Wei, S., Fielding, E., Leprince, S., Sladen, A., Avouac, J.-P., Helmberger, D., … Briggs, R. (2011). Superficial simplicity of the 2010 El Mayor–Cucapah earthquake of Baja California in Mexico. *Nature Geoscience*, *4*(9), 615–618.

Weng, H., & Yang, H. (2017). Seismogenic width controls aspect ratios of earthquake ruptures. *Geophysical Research Letters*, *44*, 2725–2732. https://doi.org/10.1002/2016GL072168

Wesnousky, S. G. (2006). Predicting the endpoints of earthquake ruptures. *Nature*, *444*(7117), 358–360.

Wesnousky, S. G., & Biasi, G. P. (2011). The length to which an earthquake will go to rupture. *Bulletin of the Seismological Society of America*, *101*(4), 1948–1950.

Xu, X., Yu, G., Klinger, Y., Tapponnier, P., & Van Der Woerd, J. (2006). Reevaluation of surface rupture parameters and faulting segmentation of the 2001 Kunlunshan earthquake (M_w7. 8), northern Tibetan plateau, China. *Journal of Geophysical Research*, *111*, B05316. https://doi.org/10.1029/2004JB003488

Yıkılmaz, M., Turcotte, D., Heien, E., Kellogg, L., & Rundle, J. (2015). Critical jump distance for propagating earthquake ruptures across step-overs. *Pure and Applied Geophysics*, *172*(8), 2195–2201.

Yue, H., Lay, T., & Koper, K. D. (2012). En echelon and orthogonal fault ruptures of the 11 April 2012 great intraplate earthquakes. *Nature*, *490*(7419), 245–249.

Zhou, Y., Walker, R. T., Elliott, J. R., & Parsons, B. (2016). Mapping 3D fault geometry in earthquakes using high-resolution topography: Examples from the 2010 El Mayor-Cucapah (Mexico) and 2013 Balochistan (Pakistan) earthquakes. *Geophysical Research Letters*, *43*, 3134–3142. https://doi.org/10.1002/2016GL067899

Zuza, A. V., Yin, A., Lin, J., & Sun, M. (2017). Spacing and strength of active continental strike-slip faults. *Earth and Planetary Science Letters*, *457*, 49–62.